Ocean Modelling 91 (2015) 112–127

Contents lists available at ScienceDirect

Ocean Modelling

journal homepage: www.elsevier.com/locate/ocemod

# Impacts of regional mixing on the temperature structure of the equatorial Pacific Ocean. Part 2: Depth-dependent vertical diffusion☆

Yanli Jia[a,*], Ryo Furue[b,a], Julian P. McCreary Jr.[a]

[a] International Pacific Research Center, University of Hawaii, Honolulu, HI, USA
[b] APL, JAMSTEC, Yokohama, Japan

ARTICLE INFO

*Article history:*
Available online 18 March 2015

*Keywords:*
Diffusion
Rossby waves
Kelvin waves
Advection
Pycnocline
Ocean general circulation models

ABSTRACT

In this study, we use an ocean model to explore how vertical mixing influences temperature in the eastern equatorial Pacific Ocean. Our approach is to change the background diffusion coefficient from a constant value $\kappa_b$ to $\kappa_b + \delta\kappa(z)$ in various subregions of the tropical Pacific, and then to determine the resulting temperature changes in the near-equilibrium response. In a companion paper (Furue et al., 2015), we consider the impacts of depth-independent $\kappa_b$ anomalies. Here, we examine the impacts of depth-dependent anomalies that are confined above, or centered on, the mid-depth of the pycnocline.

During the first year of adjustment, solutions develop a local temperature response that results largely from the one-dimensional balance $\delta T_t = (\delta\kappa T_z)_z = \delta\kappa_z T_z + \delta\kappa T_{zz}$, with a similar equation for salinity. At this stage, $\delta\kappa$ generates temperature and salinity anomalies that are either associated with a density change (dynamical anomalies) or without one (spiciness anomalies). Subsequently, dynamical and spiciness anomalies spread to remote regions by wave radiation and advection, respectively.

For positive $\delta\kappa$ anomalies confined above the mid-pycnocline, $\delta\kappa_z T_z$ tends to produce positive temperature anomalies, which spread to the equator dynamically (by wave radiation) and are still apparent in near-equilibrium solutions. For $\delta\kappa$ anomalies confined within the pycnocline (with monopole, dipole, and tripole profiles), the response is dominated by $\delta\kappa_z T_z$, owing to $\delta\kappa$ having a smaller vertical scale than $T$ and to the depth range where $\delta\kappa$ is large not overlapping well with that where $|\, T_{zz}\,|$ is; the resulting temperature anomalies tend to shift the pycnocline vertically (dipole profile) or to alter its thickness (monopole and tripole profiles).

Positive anomalies from all subregions contribute to an increase of near-surface(upper 50 m) temperature in the eastern equatorial Pacific, the amplitude and location of the warming depending on the depth range of the warming band generated within the locally forced subregion.



## 1. Introduction

### 1.1. Background

Vertical diffusion in the ocean is a critical process that impacts many oceanic phenomena. In the tropical Pacific Ocean, diffusion affects equatorial, sea-surface temperature (SST) either directly via mixed-layer processes or indirectly through its influence on the temperature of the water that upwells in the eastern, equatorial Pacific Ocean (EEPO); as a consequence, it can also influence ocean–atmosphere interaction and climate variability (e.g., Meehl et al., 2001; Richards et al., 2009; Sasaki et al., 2013). Despite its known importance, the magnitude of diffusion is unclear, a result of its being highly variable in space and time. It is essential to determine just how this variability impacts the ocean state, and to improve oceanic mixing parameterizations to allow for it.

#### 1.1.1. Observations

There have been a number of observational analyses that estimate the vertical diffusion coefficient, $\kappa$, in various oceanic regions. For example, based on tracer distributions in the pycnoclines of the North Atlantic and North Pacific, the spatially averaged value of $\kappa$ is estimated to be of the order of $10^{-5}$ m$^2$/s (Ledwell et al., 1998; Kelley and Van Scoy, 1999). Using strain information from Argo profiles, Whalen et al. (2012) provide maps of dissipation rate and vertical diffusivity for 250–2000 m, relating regions of heightened mixing to energy input from winds and tides and confirming

☆ This manuscript is SOEST Contribution 9267 and IPRC Contribution 1101.

* Corresponding author at: International Pacific Research Center, University of Hawaii, Honolulu, HI, USA.
*E-mail address:* yjia@hawaii.edu (Y. Jia).

http://dx.doi.org/10.1016/j.ocemod.2015.02.007

previous observations of locally intensified mixing above regions of rough topography. Among other things, their maps show elevated mixing in the Northwest Pacific (north of 20°N) that results from winter storm activity. Sriver and Huber (2007) reported a similar mixing enhancement in the upper tropical oceans due to summertime, tropical-cyclone activity.

In the equatorial Pacific, vertical-mixing values are low near the core of the Equatorial Undercurrent (EUC), a consequence of the low current shear and high stratification there, whereas values are larger above the EUC core due to greater current shear (Jones, 1973; Gregg, 1976; Gregg et al., 1985; Moum et al., 1989; Kanari et al., 1992). Some measurements also indicate a moderate increase of mixing below the EUC core, where the stratification is relatively weaker and shear larger (Jones, 1973; Gregg, 1976; Gregg et al., 1985; Whalen et al., 2012; Richards et al., 2012). Upper-ocean mixing may be further enhanced in the equatorial Pacific by shear associated with tropical instability waves (TIWs; Moum et al., 2009) and in small-vertical-scale velocity structures (Richards et al., 2012).

*1.1.2. Models*

Many numerical modeling studies have demonstrated the sensitivity of the large-scale ocean circulation to global changes of $\kappa$ (e.g., Bryan, 1987; Cummins et al., 1990). Recently, a number of studies have begun to explore how changes of $\kappa$ in specific oceanic regions impact the near-equatorial circulation and stratification. For example, Sasaki et al. (2012) increased the background diffusion coefficient, $\kappa_b$, above the middle of the thermocline (~20°C) in the equatorial Pacific, as a way of accounting for enhanced mixing by small-vertical-scale velocity structures (Richards et al., 2012); they found that the thermocline is sharpened, the stratification above the thermocline is reduced, and the eastern cold tongue is warmed through air-sea feedback mechanisms, leading to an improved, equatorial SST distribution. Sriver and Huber (2010), Fedorov et al. (2010), Manucharyan et al. (2011) and others explored effects of enhanced $\kappa$ in extra-tropical regions induced by tropical cyclones; they found that increased $\kappa$ in the upper ocean warms subsurface waters locally, and hypothesized that they are then advected to the equator within the subsurface branch of the Subtropical Cells, eventually upwelling to the surface in the EEPO.

Using a model of the tropical Pacific, Furue et al. (2015) systematically examined the ocean's response to $\kappa_b$ anomalies that were depth independent and confined to specific geographic regions (see Fig. 1 below). They noted that adjustments to an imposed $\delta\kappa$ take place in three steps: (1) a rapid (few weeks) initial response involving interactions of swiftly propagating, gravity and barotropic waves with eddies, which generates small-scale temperature anomalies throughout the domain; (2) a gradual (~1 yr) local response within the forced region that is well represented by a one-dimensional (1-d) vertical diffusive balance (see Eq. 1 below); and (3) a slow (5 or more years) response during which local temperature anomalies spread to the equator. The authors split locally-generated temperature anomalies into two parts: one that arises from the vertical displacement of density (dynamical anomalies), and the other that occurs when temperature and salinity changes compensate so that density remains unchanged (spiciness anomaly). This split is useful because the two anomaly types spread to remote regions by different mechanisms, the former by wave radiation and the latter by advection. The vertical structure and amplitude of the local anomalies differs significantly from subregion to subregion, and hence so does their impact on equatorial temperatures.

To explore the spatial variability of $\kappa$, Liu et al. (2012) assimilated data into their global ocean model. Specifically, $\kappa$ is initially assigned a constant value of $\kappa_0 = 10^{-5}$ m$^2$/s, which is subsequently

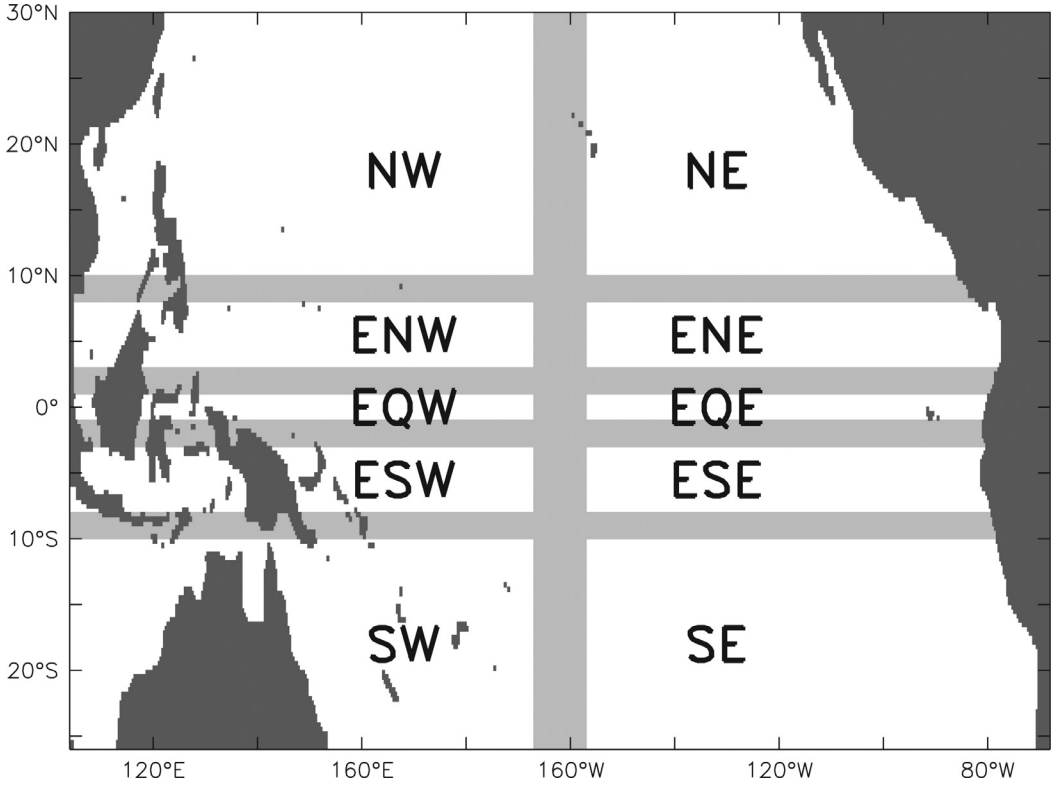


**Fig. 1.** The model domain showing the geographical regions where $\kappa_b$ anomalies are imposed. The gray bands are ramp regions, within which $\kappa_b$ is ramped sinusoidally from a reference value, $\kappa_r$, outside the region ($\kappa_r = \kappa_0$ and $5 \times 10^{-5}$ m$^2$/s for the solutions in Sections 3 and 4, respectively) to $\kappa_r + \delta\kappa$ inside the region.

adjusted to $\kappa_0 + \delta\kappa$ in order to obtain a solution that best fits observed temperature, salinity, and other variables. Significant changes in $\kappa$ are typically collocated with temperature fronts. In the tropical Pacific, $\delta\kappa$ exhibits a "tripole" pattern, with negative values near the middle of the pycnocline and positive values just above and below. It is difficult to assess in their solution whether $\delta\kappa$ is generated to represent mixing distributions in the real ocean more faithfully or to compensate for model errors. In the tropical Pacific, however, the fact that tripole pattern is consistent with the observed mixing profiles noted in Section 1.1.1 suggests that it captures some real depth variations.

### 1.2. Present research

In this study, we continue to explore the impacts of $\kappa_b$ on the tropical-Pacific stratification. Specifically, our goal is to determine the precise physical mechanisms that account for the EEPO warming resulting from enhanced upper-ocean mixing as reported by Fedorov et al. (2010), Manucharyan et al. (2011), and Sasaki et al. (2012), and to provide a physical interpretation of why certain $\delta\kappa$ structures develop in the best-fit solution of Liu et al. (2012). Following Furue et al. (2015), we obtain solutions to an ocean general circulation model (OGCM) in which $\kappa_b$ is changed in various subregions of the tropical Pacific, and then assess the resulting temperature changes in the near-equilibrium response. In contrast to that study, however, we consider impacts of depth-dependent anomalies that are confined above, or centered on, the mid pycnocline. To understand basic effects of $\delta\kappa$, we also find analytic solutions to a simplified, one-dimensional (1-d) version of the model (Appendix A).

Key results are the following. During the initial adjustment to a mixing anomaly $\delta\kappa$, solutions develop a local temperature response that is generated either by $\delta\kappa_z T_z$ or $\delta\kappa T_{zz}$. For positive $\delta\kappa$ anomalies above the mid-pycnocline, $\delta\kappa_z T_z$ tends to produce local positive temperature anomalies whereas $\delta\kappa T_{zz}$ tends to produce negative ones; further, both forcings primarily generate dynamical anomalies that spread to the equator by wave radiation. For $\delta\kappa$ anomalies confined within the pycnocline, the resulting temperature anomalies are almost entirely caused by $\delta\kappa_z T_z$, and they tend to shift the pycnocline vertically or to alter its thickness. In near-equilibrium solutions, the positive anomalies from all subregions rise to the surface in the EEPO, where they contribute to warming the cold tongue there.

The paper is organized as follows. Section 2 describes our overall experimental design. Sections 3 and 4 report solutions for $\kappa_b$ anomalies located above and within the pycnocline, respectively, and Appendix A derives analytic, 1-d solutions that illustrate their basic properties. Section 5 provides a summary and discussion.

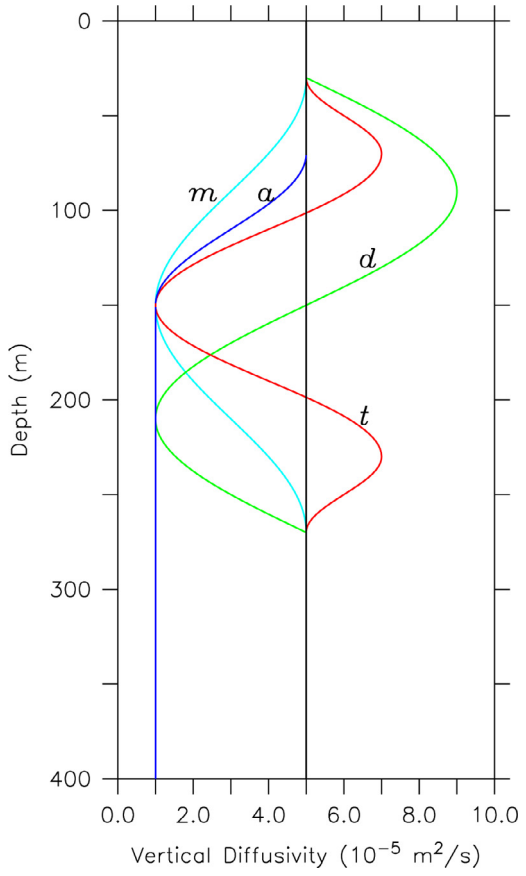


**Fig. 2.** Profiles of the background vertical diffusivity, $\kappa_b$, showing the FB-run profile (black line), and the four profiles used in the sensitivity experiments, when the depth of the 25.0-$\sigma_\theta$ density surface is at $z_0 = -150$ m. In experiments labeled *a*, the diffusivity is the blue curve below $z = -70$ m and follows the black line above. In experiments labeled *m*, *d*, and *t*, the diffusivity is the cyan, green, and red curve, respectively from 30–270 m, and follows the black line elsewhere. Profiles *a*, *m*, and *d* are composed of a single sinusoidal curve; profile *t* is composed of three sinusoidal curves from 30–70 m, 70–230 m, and 230–270 m. (For interpretation of the references to color in this figure legend, the reader is referred to the web version of this article.)

## 2. Experimental design

Here, we describe our ocean model (Section 2.1), report the experiments that we carry out (Section 2.2), and define the various measures of solution differences that we use (Section 2.3). Our overall experimental design is essentially the same as that of Furue et al. (2015); additional model details and other relevant information can be found there.

### 2.1. Ocean model

Our ocean model is a version of the Massachusetts Institute of Technology general circulation model (MITgcm; Marshall et al., 1997), which solves the incompressible Navier–Stokes equations on a sphere. Subgrid-scale horizontal mixing is parameterized by biharmonic operators with constant coefficients of $4 \times 10^{11}$ m$^4$/s for viscosity and $2 \times 10^{11}$ m$^4$/s for tracer diffusion. The K-profile parameterization of Large et al. (1994) is used for vertical mixing, with background coefficients of $10^{-4}$ m$^2$/s for viscosity and $\kappa_b = \kappa_0 + \delta\kappa$ for diffusion, where $\kappa_0 = 10^{-5}$ m$^2$/s and $\delta\kappa(z)$ is defined in Section 2.2.

The model domain extends over the region 26°S–30°N, 104°E–70°W, which covers the tropical and subtropical Pacific and includes a small portion of the eastern Indian Ocean. The ocean depth and continental boundaries are defined by the ETOPO2 database (http://www.ngdc.noaa.gov/mgg/global/etopo2.html), the continental boundaries determined by the 10-m bottom contour (except for singular points). The model grid has a constant horizontal resolution of 1/3° both zonally and meridionally, and the vertical grid has 51 levels with a resolution that ranges from 5 m near the surface to 510 m near the bottom. No-slip conditions are applied at all continental boundaries. Along the artificial boundaries at 26°S, 30°N, and 104°E, model variables (temperature, salinity, and horizontal velocity) are relaxed to a monthly climatology determined from the German partner of the consortium for Estimating the Circulation and Climate of the Ocean (GECCO) reanalysis (Köhl et al., 2007; Köhl and Stammer, 2008), with a time scale that varies from 1–20 days within 3° of the boundaries.

Surface forcing fields (wind stress and heat and fresh water fluxes) are computed from a monthly climatology of atmospheric

variables based on the bulk formulae of Large and Pond (1981) and Large and Pond (1982). The climatology was produced with the European Centre for Medium Range Weather Forecasts (ECMWF) Interim Reanalysis (ERA-Interim, http://apps.ecmwf.int/datasets/data/interim-full-daily).

### 2.2. Experiments

Solutions are obtained as follows. As in Furue et al. (2015), we first initialize the model with the January climatology of the GECCO reanalysis and then integrate it for 40 yr, by which time the response is close to equilibrium. In Section 3, solutions are initialized with this background state and integrated for 20 yr. In Section 4, they are initialized with the 20-yr state of Experiment FB (defined next) and integrated for 20 yr. For each experiment, we define the start time of its integration to be $t = 0$. Then, the initial and near-equilibrium responses of the solutions shown in Sections 3 and 4 are from year 1 or year 20, respectively.

Our control run (Experiment CTL) has $\delta\kappa = 0$, that is, it is an extension of the spin-up integration for an additional 20 yr. Experiment FB has $\delta\kappa = 4 \times 10^{-5}$ m$^2$/s, so that $\kappa_b$ is increased everywhere to $5 \times 10^{-5}$ m$^2$/s. In other sensitivity runs, $\delta\kappa$ is confined to the geographical subregions shown in Fig. 1 and varies in $z$ (profiles $a$, $m$, $d$, and $t$ discussed next). We label these runs by the subregion where $\delta\kappa$ is imposed and by the vertical profile of $\delta\kappa$. For example, the run with $\kappa_b$ imposed in Region EQW that uses profile $a$ is "Experiment EQW$a$." Solution names without a profile index designate experiments in which $\delta\kappa$ is depth-independent, for example, as in "Experiment EQW"; these solutions are the same as those reported in Furue et al. (2015).

Vertical profiles of $\delta\kappa$ are prescribed relative to the mean 25.0-$\sigma_\theta$ potential-density surface, $z_0(x, y)$, which lies roughly along the middle of the pycnocline in the equatorial Pacific. Near the equator, this isopycnal surface shoals from about 150 m in the west to about 30 m in the east (e.g., Fig. 3), and it outcrops near the southeast corner of the domain. Fig. 2 displays the $\kappa_b$ profiles we use at a location where the depth of the 25.0-$\sigma_\theta$ surface is $z_0 = -150$ m. At other locations, the profiles are shifted vertically, with values of $z_0$ following the 25.0-$\sigma_\theta$ surface from the year-1 average of Solution CTL for solutions with profile $a$, and an equivalent surface obtained from the year-21 average of Solution FB for profiles $m$, $d$, and $t$.

For experiments CTL and FB, $\kappa_b = 1 \times 10^{-5}$ m$^2$ s$^{-1}$ (not shown) and $\kappa_b = 5 \times 10^{-5}$ m$^2$ s$^{-1}$ (black line). In all other experiments, it has one of four, $z$-dependent profiles. Profile $a$ follows the blue curve with $\kappa_b$ increasing from $1 \times 10^{-5}$ below $z = -150$ m to $5 \times 10^{-5}$ m$^2$ s$^{-1}$ above $z = -70$ m. Profiles $m$, $d$, and $t$ have monopole, dipole, and tripole structures, respectively, from $z = -270$ m to $z = -30$ m and follow the black line elsewhere. These profiles are motivated by the studies noted in the introduction. Profile $a$ represents an increase in upper-ocean mixing due to tropical storms, small-scale structures, and TIWs. Profiles $m$, $d$, and $t$

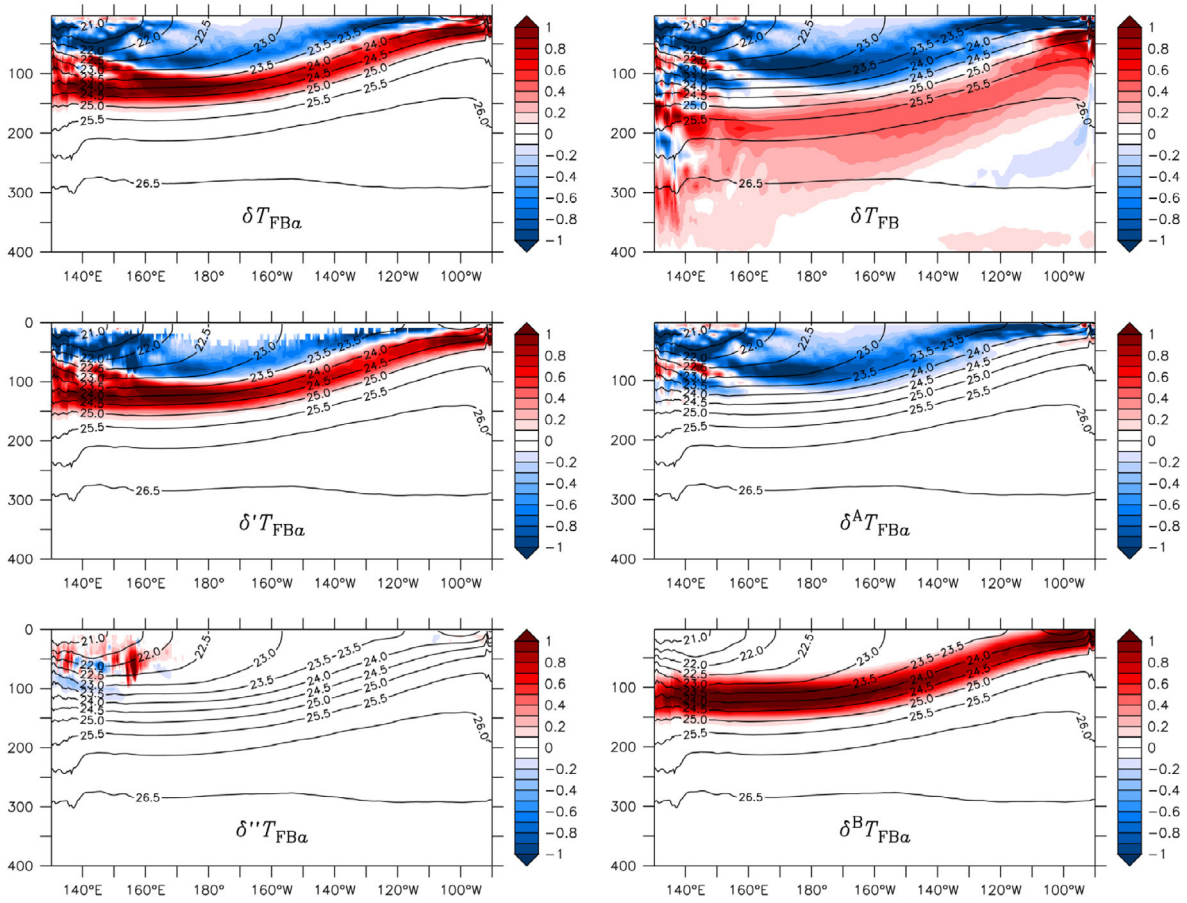


**Fig. 3.** Sections of temperature anomalies (°C) along the equator (1°S–1°N average) evaluated using (1) at $t = 6$ months: the total anomaly for Experiment FB (top-right); that for Experiment FB$a$ (top-left), its dynamical and spiciness components (middle- and bottom-left panels), and its $\delta\kappa\, T_{0zz}$ and $\delta\kappa_z T_{0z}$ components (middle- and bottom-right panels). In Experiment FB, $\kappa_b$ is increased everywhere to a constant value over the entire water column, whereas in Experiment FB$a$ it is increased only above the mean 25-$\sigma_\theta$ surface (see Section 3.1 for details).

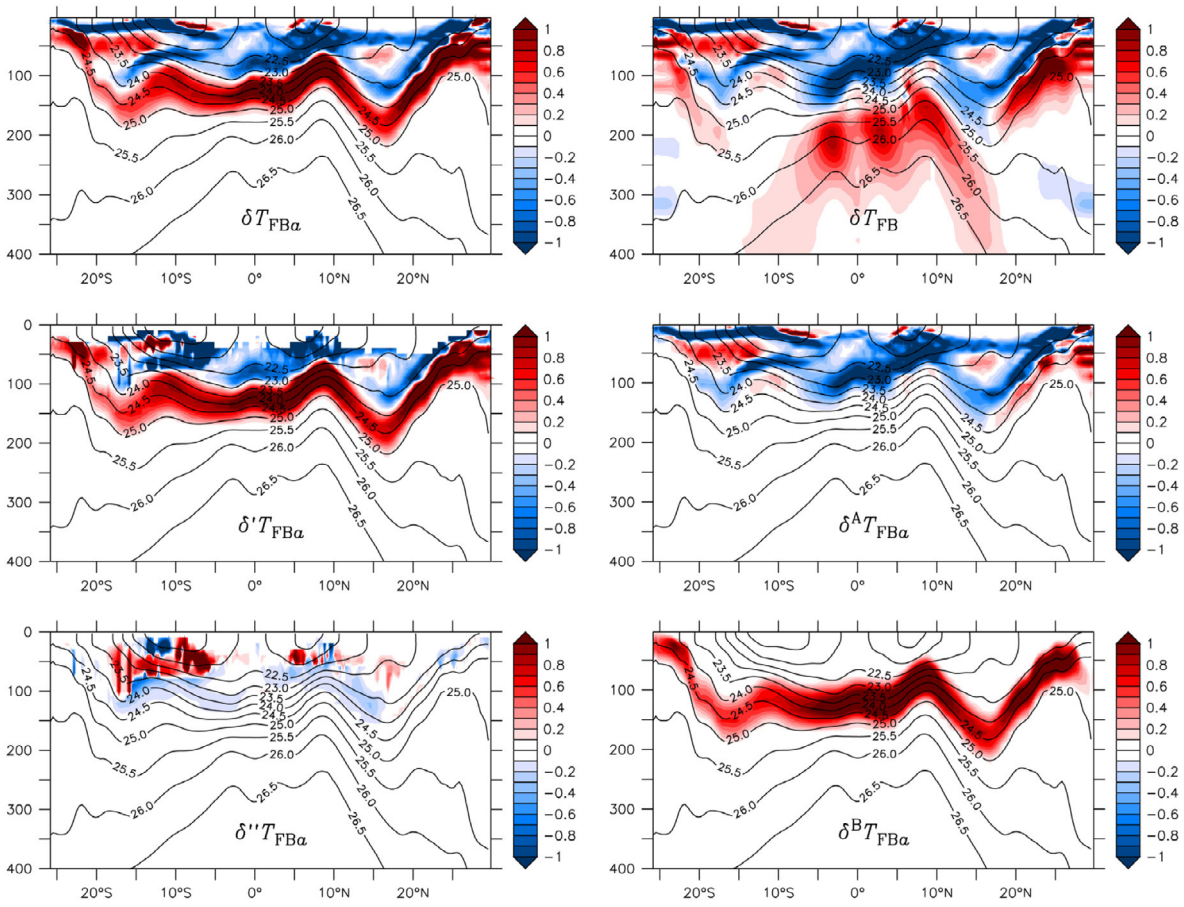


**Fig. 4.** As for Fig. 3, but for sections along 170°E.

represent the more complex structures that can develop due to shear instabilities of EUC and that appear in Liu et al. (2012) solution.

### 2.3. Difference measures

For the runs that use profile *a* (Section 3), we define the temperature anomalies generated by $\delta\kappa$ within Region $e$ ($e$ = NE, EQW, …) to be the temperature difference between Experiments $e$ and CTL, $\delta T_e \equiv T_e(x,y,z,t) - T_{\mathrm{CTL}}(x,y,z,t)$. For the other runs (Section 4), the temperature anomalies are $\delta T_e \equiv T_e(x,y,z,t) - T_{\mathrm{FB}}(x,y,z,t')$, where $t' = t + 20$ yr and $t$ varies from 0 to 20 yr.

Following Furue et al. (2015), we separate $\delta T_e$ into dynamical ($\delta' T_e$) and spiciness ($\delta'' T_e$) parts. The initial response of $\delta T_e$ can also be separated in another, instructive way. Initially, $\delta T_e$ evolves primarily according to the 1-d (local) balance (A.2b), which, at times small enough for the last two terms to be negligible, has the solution

$$\delta T_e = (\delta\kappa_e T_{0z})_z t = \delta\kappa_e T_{0zz} t + \delta\kappa_{ez} T_{0z} t, \tag{1}$$

where $T_0 \equiv T_{\mathrm{CTL}}(x,y,z,0)$ or $T_{\mathrm{FB}}(x,y,z,20\ \mathrm{yr})$ for runs that use profile *a* or the other profiles, respectively. Eq. (1) splits $\delta T_e$ into the components $\delta^A T_e \equiv \delta\kappa_e T_{0zz} t$ and $\delta^B T_e \equiv \delta\kappa_{ez} T_{0z} t$. Although defined only for the initial response, the two components are clearly identifiable in near-equilibrium solutions. As we shall see, the additional term $\delta^B T_e$, which exists because $\delta\kappa_{ez} \neq 0$, significantly impacts temperature anomalies, even changing their sign. (Furue et al. (2015) discuss a similar balance, except without the last term in Eq. (1) since $\delta\kappa_{ez} = 0$ for their depth-independent mixing anomalies.)

## 3. Solutions for upper-ocean $\delta\kappa$

In this section, we report the temperature anomalies that develop in sensitivity experiments when $\kappa_b$ is increased above the mid-pycnocline (profile *a* in Fig. 2). First, we discuss Experiment FB*a*, which provides an overview of the locally forced responses that occur in all the regional solutions (Section 3.1). Then, to illustrate remote impacts, we discuss the anomalies for several of the regional experiments (Section 3.2). For each experiment, we begin with a discussion of anomaly generation by the 1-d process (1) and then describe how the anomalies propagate out of the forced region. As we shall see, this approach is useful because the 1-d mechanism determines not only the initial local response but also the long-term local response and ultimately the remote response through the propagation of the signals from the locally-forced region. The characteristics of initial 1-d response in a subregion are therefore key to understand the complete response.

### 3.1. Experiment FBa

Figs. 3 and 4 show the initial (6 month) development of temperature anomalies determined by (1) when $\delta\kappa$ has profile *a* throughout the basin, that is, the response is the theoretical analog of Experiment FB*a*. With a few exceptions, the $\delta T_{\mathrm{FB}a}$ signal (Figs. 3 and 4, top-left panels) consists of warming within the pycnocline and near-surface cooling. Comparing the left panels shows that

almost all of the signal is dynamical ($\delta' T_{\mathrm{FB}a}$; middle-left panels) with only weak spiciness anomalies occurring south of 8°S and from the equator to about 15°N ($\delta'' T_{\mathrm{FB}a}$; bottom-left panels). Comparing the top-left, middle-right, and bottom-right panels shows that most of the warming and all of the cooling in $\delta T_{\mathrm{FB}a}$ is generated by $\delta\kappa_z T_{0z} t$ ($= \delta^B T_{\mathrm{FB}a}$) and $\delta\kappa T_{0zz} t$ ($= \delta^A T_{\mathrm{FB}a}$), respectively. Consistent with its definition, $\delta^B T_{\mathrm{FB}a}$ (bottom-right panel) is confined to the region where $\delta\kappa_z \neq 0$ and is everywhere positive since $\delta\kappa_z > 0$ and $T_{0z} > 0$. The importance of $\delta\kappa_z$ in producing warm anomalies is confirmed by the temperature anomalies in Experiment FB for which $\delta\kappa_{\mathrm{FB}}$ is depth-independent (top-right panels): The warming band has a very different structure within 15° of the equator, being more diffuse with a maximum in the lower, rather than mid-, pycnocline.

Fig. 5 plots the year-1 average of temperature anomalies from Experiment FB*a*, a counterpart to the 6-month response based on (1). Their distributions closely follow their 1-d counterparts in Figs. 3 and 4, but their amplitudes are lower due to the presence of additional processes (wave radiation, advection, and mixing) not accounted for in (1) (see Appendix A). A notable structural difference is that the region of upper-ocean warming in the EEPO is thicker in Experiment FB*a* (compare top-left panels in Figs. 5 and 3), weakening or eliminating the near-surface cooling there. This difference is likely a dynamical adjustment caused by the swift, eastward propagation of equatorial Kelvin waves and their initial reflection from the eastern boundary as Rossby waves (see the discussion of Fig. 7, Section 3.2).

Fig. 6 shows the year-20 temperature anomalies for Experiment FB*a*. The warming patterns are similar to those for year 1 (Fig. 5), except that their amplitudes are larger and their vertical extent in the EEPO is greater. In addition to warming, a negative spiciness anomaly also develops within the pycnocline (bottom panels). Along the equator, the cooling signal is much stronger than it is initially, in part because of the longer integration time but primarily due to advection from off-equatorial regions (bottom-right panel of Figs. 5 and 6); nevertheless, in the total anomaly $\delta T_{\mathrm{FB}a}$ (top panels) it is mostly overwhelmed by the positive dynamical anomaly (middle panels) and does not affect near-surface temperatures in the EEPO. In contrast to the warm band, the spiciness signal (Fig. 6, bottom panels) remains mostly confined in the depth range of the forcing and weakens to the east; at the eastern boundary it only downwells, a consequence of its being located deeper than the upwelling depth.

Another noteworthy feature in Fig. 6 is the positive, spiciness anomaly below the pycnocline in Region SW (bottom-right panel), which is too deep to be generated by local forcing. It is likely associated with the negative, dynamical anomaly in the same region, which is remotely generated by the propagation of damped Rossby waves into the region. Because this dynamical signal occurs in a region of significant salinity variations (Fig. 4b of Furue et al. (2015), and their discussion of the figure in their Section 3.2.2), it leads to the spiciness response. Finally, small-scale variations are apparent in the longitudinal sections; they result from interactions

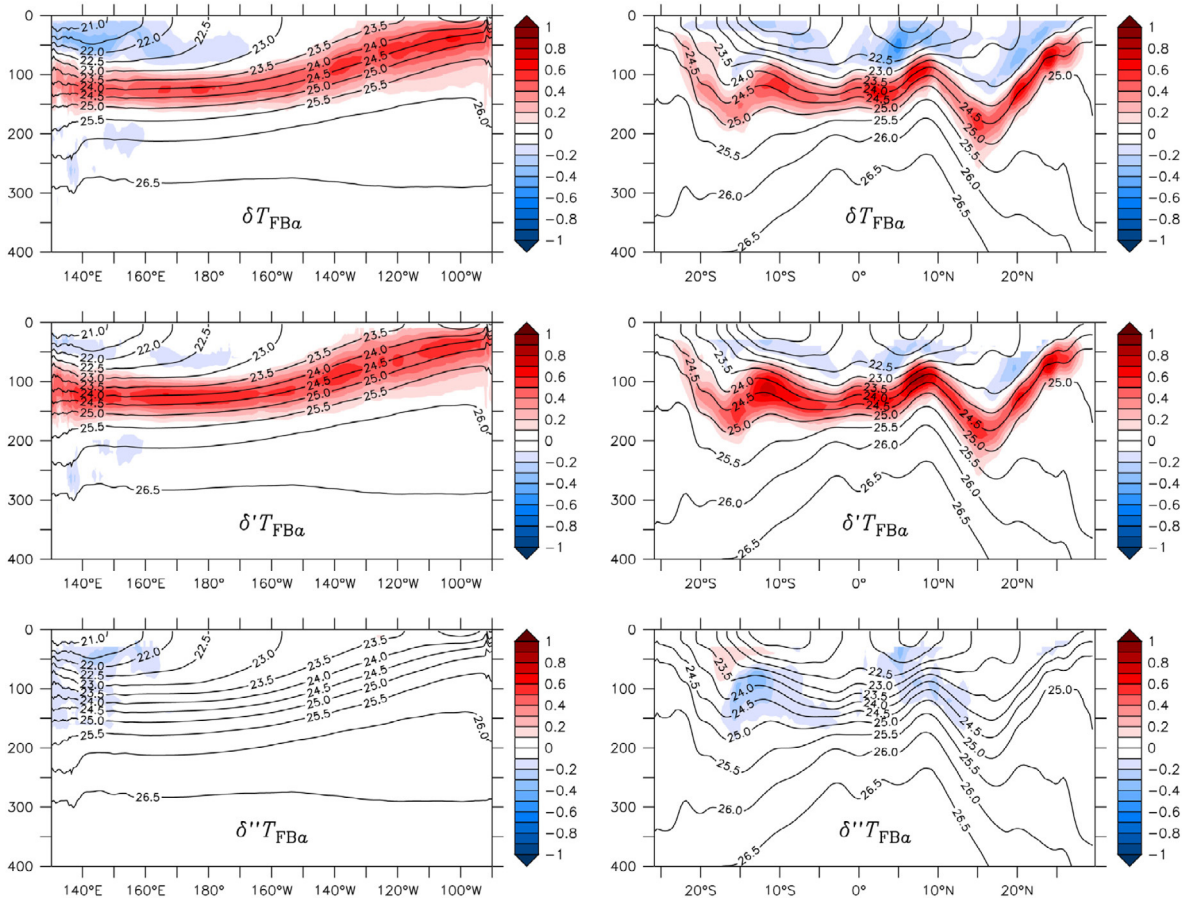


**Fig. 5.** Sections of actual temperature anomalies (°C) along the equator (1°S–1°N average; left panels) and 170°E (right panels) averaged over year 1 of Experiment FB*a*. Note that the temperature anomaly shown in each panel includes contributions from all processes, whereas its counterpart in Fig. 3 or Fig. 4 includes only the 1-d process evaluated using (1) (see Section 3.1 for a detailed comparison).

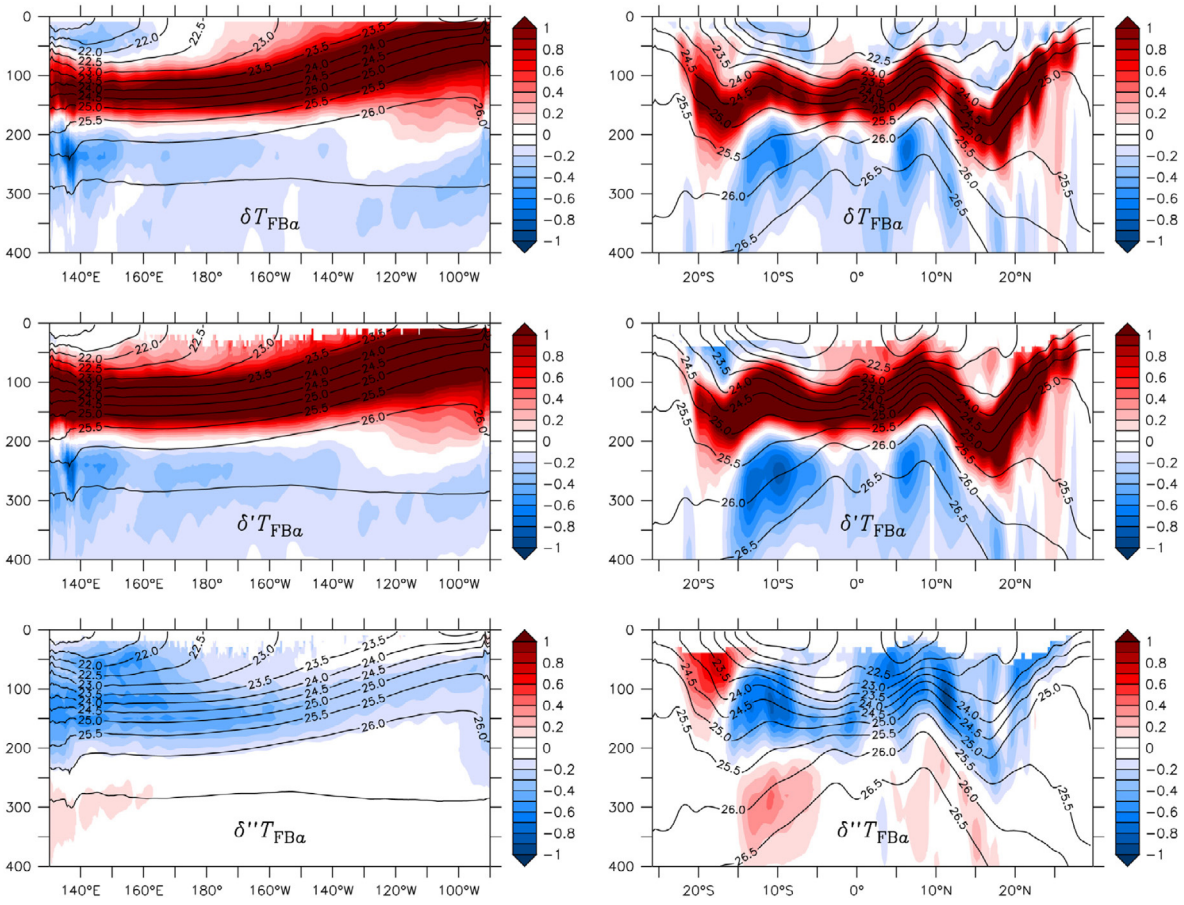


**Fig. 6.** As for Fig. 5, except averaged over year 20 of Experiment FB*a*.

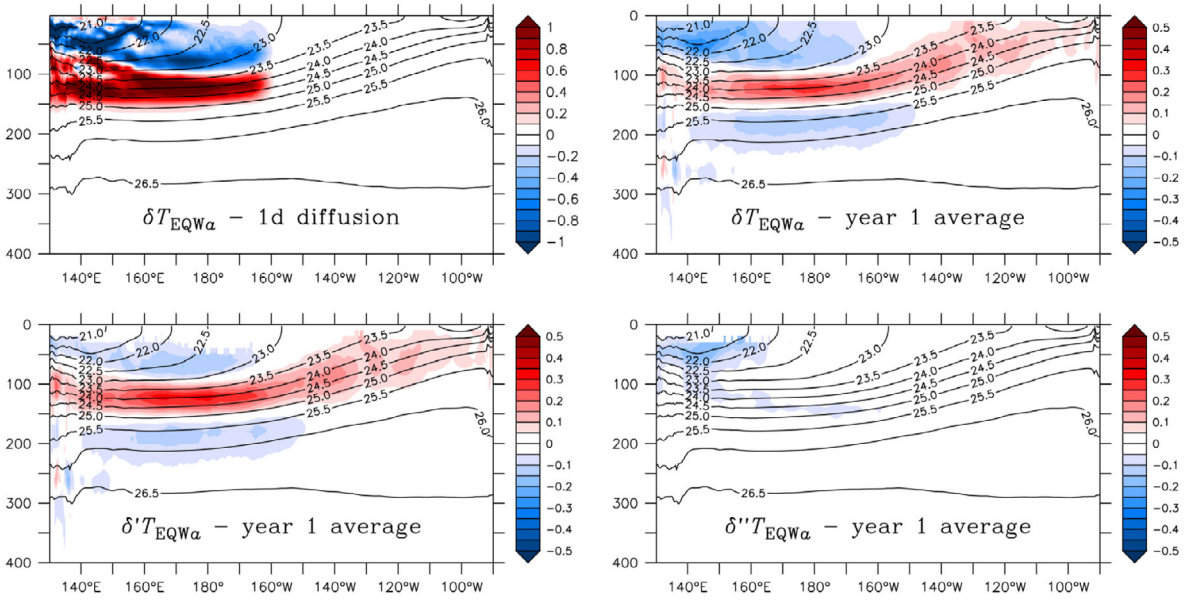


**Fig. 7.** Sections of temperature anomalies (°C) along the equator (1°S–1°N average), showing the 1-d response at 6 months (top-left panel) and year-1 averages of $\delta T_{EQWa}$, $\delta' T_{EQWa}$, and $\delta'' T_{EQWa}$.

of the large-scale signals with small-scale eddies and current bands (Section of Furue et al. (2015)).

### 3.2. Regional experiments

In the regional experiments, even though the initial (year-1) temperature anomalies are confined to a particular subregion, their structure is still similar to that in Experiment FB*a* within that subregion. A notable exception occurs for Experiment EQW*a*. Fig. 7 plots equatorial anomalies from that solution, showing the 1-d response from (1) at 6 months (top-left panel) and year-1 averages of $\delta T_{\mathrm{EQW}a}$, $\delta' T_{\mathrm{EQW}a}$, and $\delta'' T_{\mathrm{EQW}a}$ (top-right, bottom-left, and bottom-right panels). The 1-d response is confined to the western ocean (top-left panel), whereas that of the numerical solution extends to the eastern ocean (top-right panel). The bottom panels demonstrate that the extension is all contained in $\delta' T_{\mathrm{EQW}a}$, indicating that it occurs dynamically via the eastward propagation of equatorial Kelvin waves.

In the near-equilibrium responses, equatorial temperature anomalies are influenced by $\kappa_b$ changes in all the subregions, a consequence of spreading by both dynamical and spiciness anomalies. Furue et al. (2015) discuss spreading processes in detail for all the subregions. Here, we illustrate them only for Experiment SW*a*. Fig. 8 plots $\delta T_{\mathrm{SW}a}$, $\delta' T_{\mathrm{SW}a}$, and $\delta'' T_{\mathrm{SW}a}$ (top, middle, and bottom panels) along the equator and 170°E (left and right panels). The locally-forced response is evident (right panels), with a structure very similar to that in Experiment FB*a* south of 10°S (Fig. 6, right panels). As discussed in Furue et al. (2015), $\delta' T_{\mathrm{SW}a}$ first spreads westward via Rossby-wave propagation to form a recirculation gyre confined largely within the latitude band of the forcing (a $\beta$-plume) and $\delta'' T_{\mathrm{SW}a}$ is advected to the western boundary by the South Pacific Subtropical Gyre. Both signals then extend to the equator along the western boundary, where they propagate eastward via Kelvin-wave radiation and advection within the EUC, respectively. Along the equator, they are both considerably weaker than they are in the forcing region: The $\delta' T_{\mathrm{SW}a}$ signal is weaker because most of it recirculates within the recirculation gyre, $\delta'' T_{\mathrm{SW}a}$ is weaker because some of it enters the Indonesian Seas to exit the basin, and both are weakened by diffusion (Furue et al., 2015).

Fig. 9 illustrates the impact of regional $\delta\kappa$ anomalies on near-surface temperatures averaged over the top 50 m, showing anomalies for Experiment FB*a* (top-left) and six of the regional experiments (middle and bottom panels). In Experiment FB*a* (top-left panel), the cold tongue warms by as much as 2°C, a consequence of the warming caused by $\delta\kappa_z$; the weak cooling in the western ocean results mostly from locally-generated spiciness anomalies (bottom panels of Fig. 6). All the subregions contribute to the cold-tongue warming. In marked contrast, when $\kappa_b$ is depth-independent there is no strong warming within the upper pycnocline, and the sign of temperature anomalies within the upper pycnocline varies from subregion to subregion (Furue et al., 2015); as a result, the cold-tongue warming is absent in Experiment FB and warming remains only in the Costa Rica dome (centered near 9°N, 90°W; Fig. 9, top-right panel).

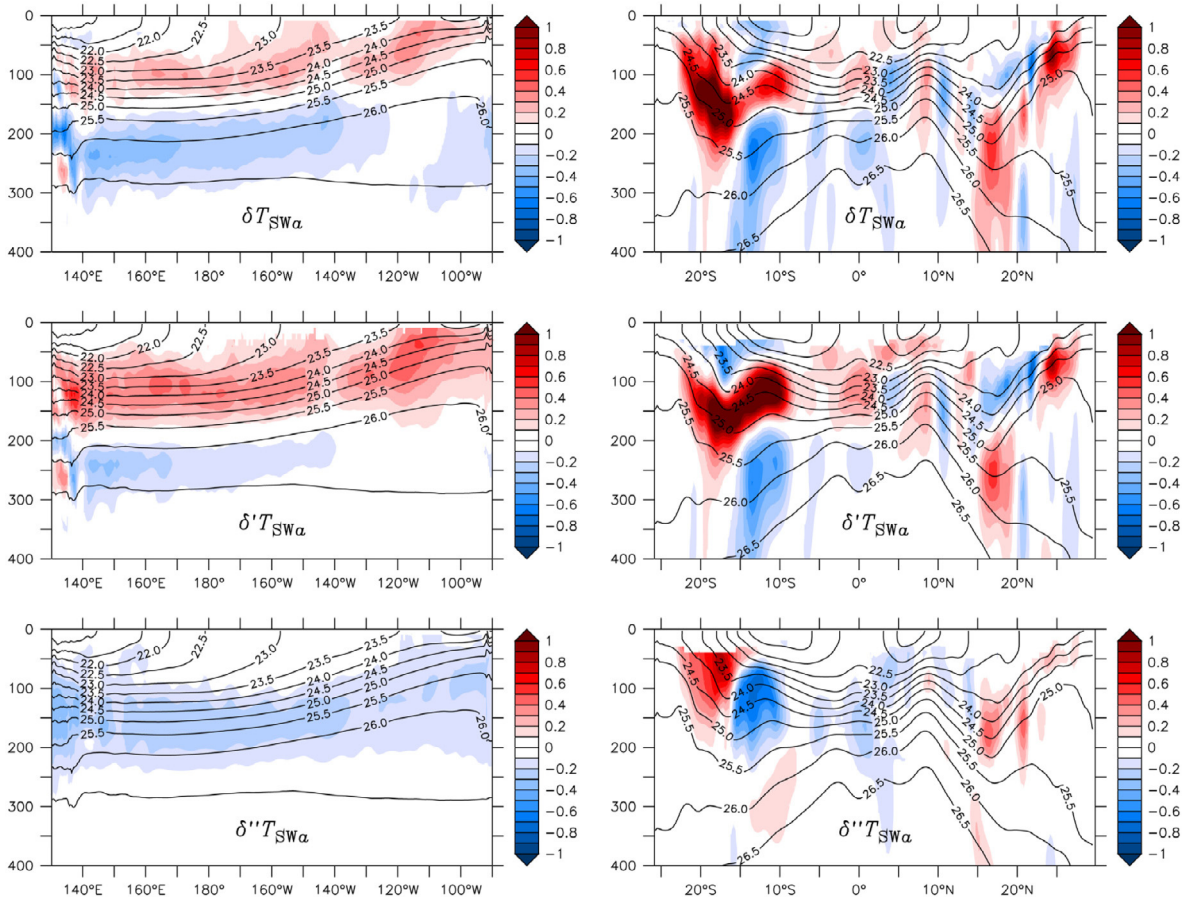


**Fig. 8.** As for Fig. 6, except for Experiment SW*a*.

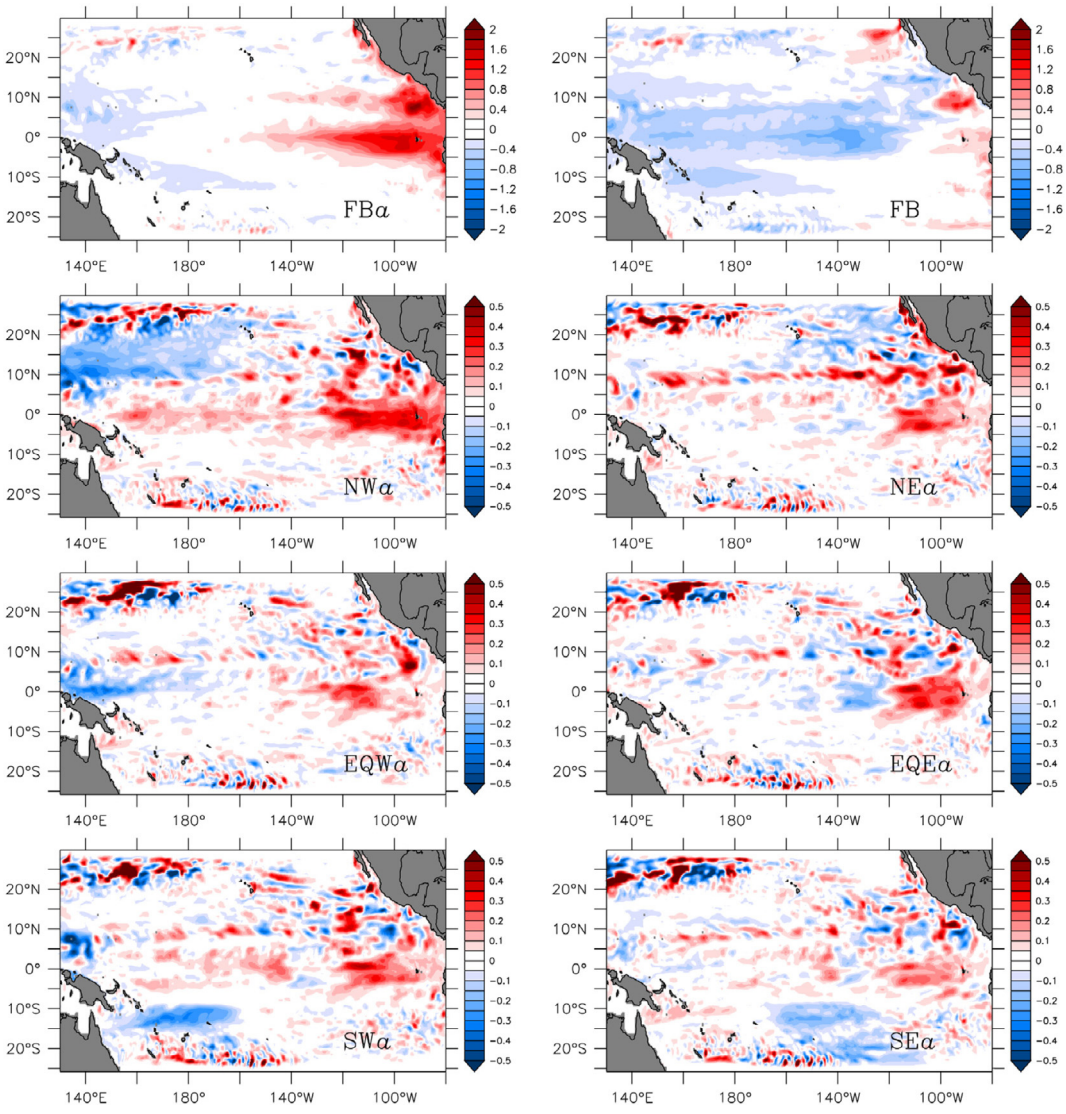


**Fig. 9.** Maps of near-surface (average in the upper 50 m) temperature anomalies (°C) during year 20 for various experiments.

Interestingly, the contribution from Experiment NW*a* to EEPO SST is largest, even more so than the contributions from Experiments EQW*a* and EQE*a*. The reason for this property is the slower adjustment time of the tropical subregions than that of the equatorial subregions, which take place by Rossby-wave and Kelvin-wave propagation, respectively; as a result, the locally forced (and subsequent remote) response in Experiment NW*a* can spin-up to a much larger magnitude (see Appendix A.2). It is also noteworthy that the EEPO SST anomaly due to Experiment SW*a* is substantially weaker than that for Solution NW*a*. The reason is that the locally generated response of Solution SW*a* has a strong, local, spiciness (cooling) response in the same depth range as the dynamical (warming) signal (Fig. 8, left panels), whereas that of Solution NW*a* does not (not shown); thus, at the equator the two signals interfere destructively in Solution SW*a*, weakening its contribution to EEPO SST.

The penetration depth of mixing anomalies due to tropical storms varies considerably, depending on the strength of the storm (100–250 m; Sriver et al., 2010). To test the impact of mixing depth on equatorial temperature anomalies, we obtained two additional experiments in Region NW, varying the mixing depth of profile *a*, $|z_0|$, from the 25.0-$\sigma_\theta$ surface (~200 m in Region NW) to shallower (24.0-$\sigma_\theta$, $\lesssim$ 150 m) and deeper (26.0-$\sigma_\theta$, $\gtrsim$ 300 m) surfaces. Fig. 10 shows the equatorial temperature anomalies in the three experiments; it also includes the anomalies from Solution NW (bottom-right panel), which essentially is the response when $|z_0|$ is beyond the ocean depth.

The plots for the three, upper-ocean mixing depths show that the equatorial thermocline is increasingly warmed as $|z_0|$ increases. The reason is because the warming signal in Region NW is generated by the term $\delta\kappa_z T_{0z}$, and hence occurs in the density range where $\delta\kappa_z \neq 0$ ($z_0 < z < z_0 + 80$ m); the resulting remote signal occurs in a similar density range, and the equatorial thermocline is most strongly affected when its density range matches best with that of the signal. When $|z_0|$ is increased further, the impact of the remote signal eventually becomes too deep to impact the equatorial pycnocline, as illustrated by Solution NW (bottom-right panel). Fedorov et al. (2010) report a similar result, in which the maximum, cold-tongue warming occurs when the mixing depth is 150–200 m. (See the discussion of Fig. 13, below, for a description of the impact of signal depth on EEPO SST in another context.)

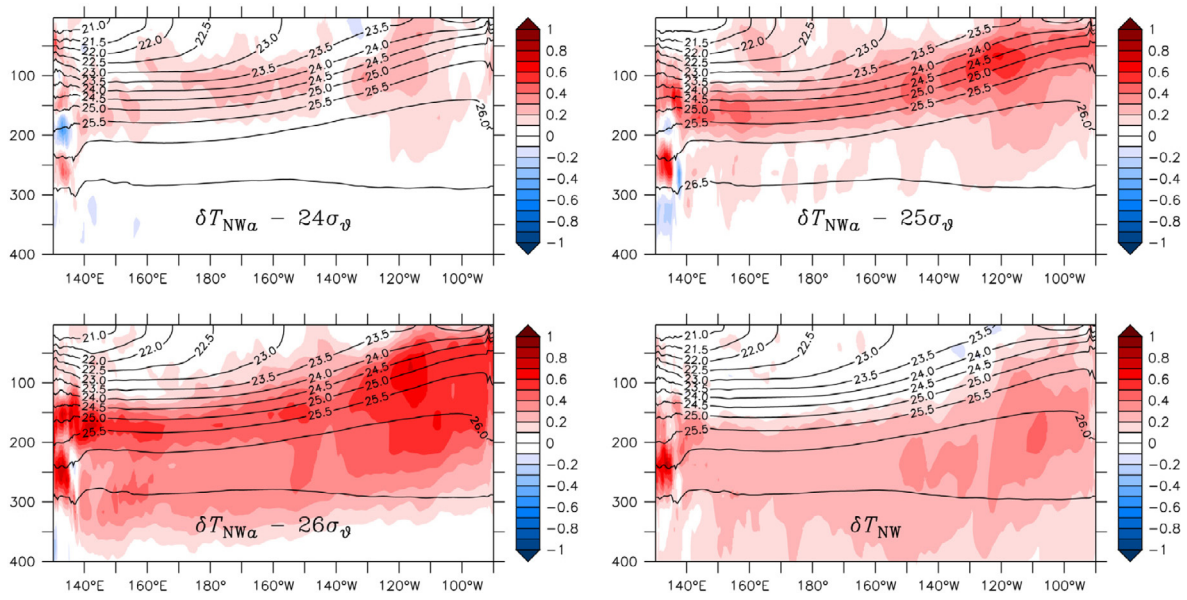


**Fig. 10.** Sections of temperature anomalies (°C) along the equator (1°S–1°N average), showing year-20 averages of $\delta T_{\mathrm{NW}a}$, when $z_0$ is located on the 24-$\sigma_\theta$, 25-$\sigma_\theta$, and 26-$\sigma_\theta$ density surfaces (top-left, top-right, and bottom-left panels), and when $|\ z_0\ |$ is essentially beyond the ocean depth ($\kappa_b$ is depth-independent; bottom-right panel). For profile *a*, the diffusivity is increased above $z_0$ (see Fig. 2).

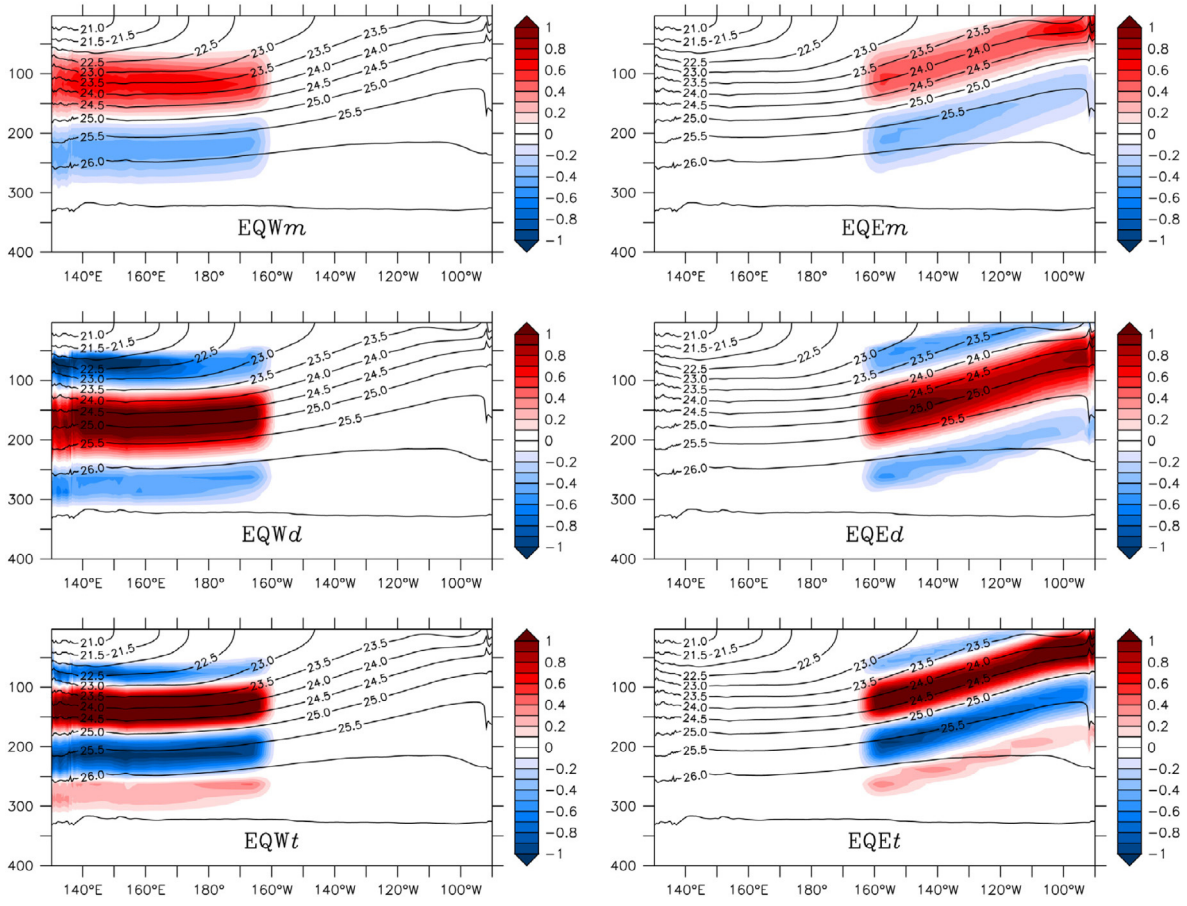


**Fig. 11.** Sections of temperature anomalies (°C) along the equator (1°S–1°N average) evaluated using (1) at $t = 6$ months, showing $\delta^B T$'s.

## 4. Solutions for $\delta\kappa$ within the pycnocline

Here, we report the responses to $\delta\kappa$ profiles that are confined to the pycnocline (profiles *m*, *d*, and *t* in Fig. 2) and to the equatorial subregions (Regions EQW and EQE). (The equatorial responses in other regional solutions have a similar structure but weaker amplitude.) Since $\delta\kappa$ for these profiles have negative, as well as positive, values, we define anomalies relative to Solution FB for which $\kappa_b$

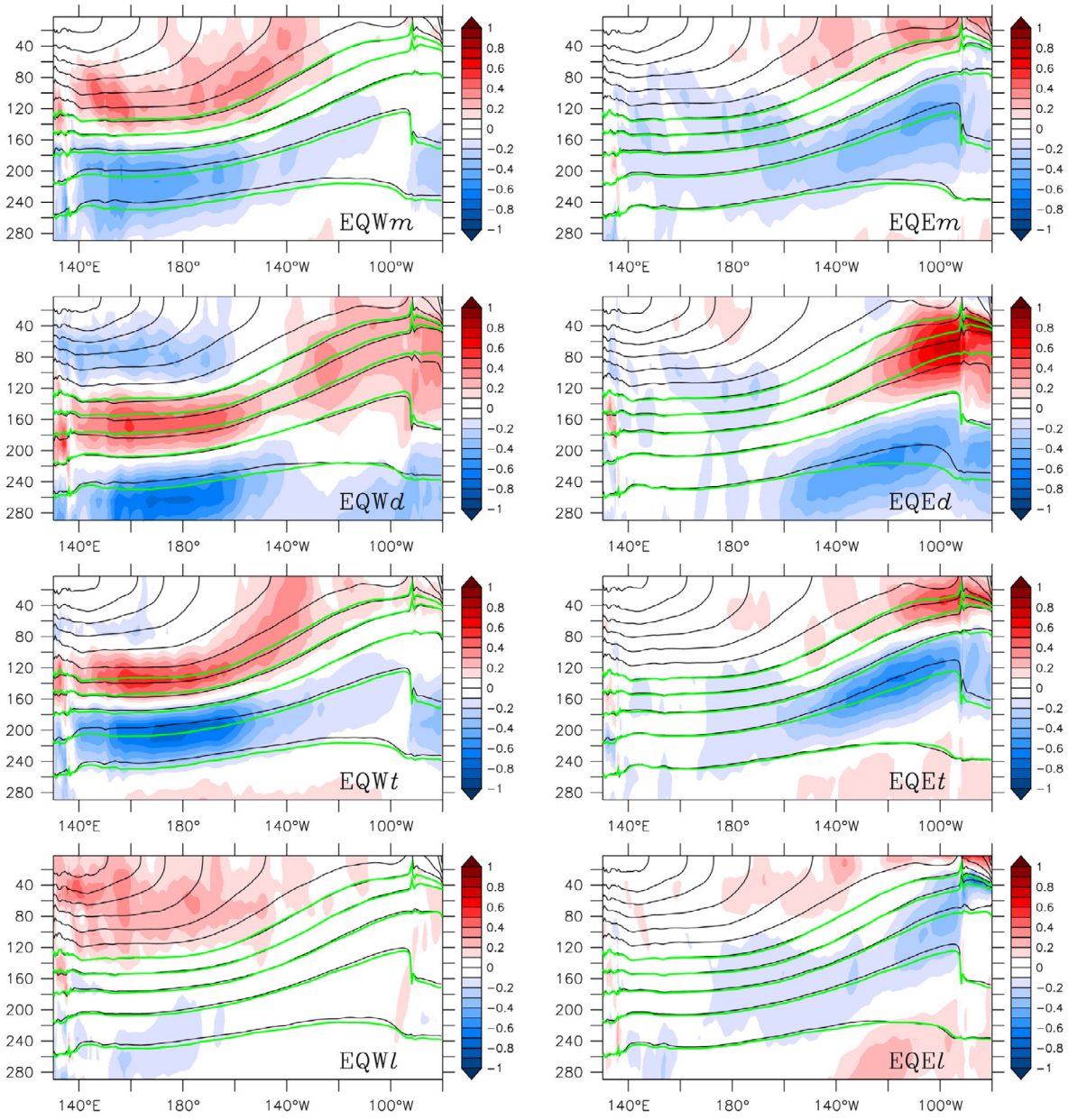


**Fig. 12.** Sections of temperature anomalies (°C, color) and density ($\sigma_\theta$, black contours) along the equator (1°S–1°N average), showing year-20 averages of $\delta T$'s. Green contours are values of $\sigma_\theta$ (24.0 to 26.0 at an interval of 0.5) from year 40 of Experiment FB (the reference experiment). Differences between the equivalent black and green contours indicate the changes of density surfaces in the sensitivity experiments. (For interpretation of the references to color in this figure legend, the reader is referred to the web version of this article.)

has the larger value of $5 \times 10^{-5}$ m$^2$/s. To supplement these numerical solutions, Appendix A reports 1-d solutions for similar $\delta\kappa$ structures. For comparison, we also report solutions with $\kappa_b$ reduced to $1 \times 10^{-5}$ m$^2$/s in the EQW and EQE regions and $\kappa_b = 5 \times 10^{-5}$ m$^2$/s elsewhere (Solutions EQW$\ell$ and EQE$\ell$, respectively).

Like solutions forced by $\delta\kappa$ anomalies with profile $a$, the temperature anomalies forced by $\delta\kappa$ with profiles $m$, $d$, and $t$ initially closely follow (1) in the forcing region and are dominated by the dynamical response ($|\ \delta' T_e\ | \gg |\ \delta'' T_e\ |$). In addition, forcing by $\delta\kappa T_{0zz}$ is weaker than that by $\delta\kappa_z T_{0z}$, because the vertical scale of $\delta\kappa$ is smaller than that of $T_0$ and because the depth ranges of $\delta\kappa$ and $T_{0zz}$ do not overlap as well as they do for $\delta\kappa_z$ and $T_{0z}$; as a result, temperature anomalies are driven mostly by $\delta\kappa_z T_{ez}$ ($|\ \delta^B T_e\ | \gg |\ \delta^A T_e\ |$). Fig. 11 shows the initial (6 month) $\delta^B T_e$ responses for Solutions EQW$i$ (left panels) and EQE$i$ (right panels), where $i = m, d, t$ (top, middle, and bottom panels). In contrast to the response using profile $a$ (Fig. 3, bottom-right panel), $\delta^B T_e$ has negative (as well as positive) bands in regions where $\delta\kappa_z < 0$. In all cases, however, there is a warm band within the pycnocline. Compared with the warm band generated by profile $a$ (Fig. 3) it is: broader, shallower, and weaker for profile $m$; broader, deeper, and more intense for profile $d$; and more intense for profile $t$. These differences all follow from the different locations and magnitudes of the positive part of $\delta\kappa_z$ for each profile.

Figs. 12 and 13 illustrate near-equilibrium $\delta T_e$ anomalies at year 20. Along the equator (Fig. 12), their similarity to the 6-month $\delta^B T_e$ responses is apparent, prominent differences being the eastward spreading of anomalies in Solutions EQW$i$ and the elimination of any cool, near-surface anomalies in Solutions EQE$i$. Because the warming bands occur at different depths across the pycnocline,

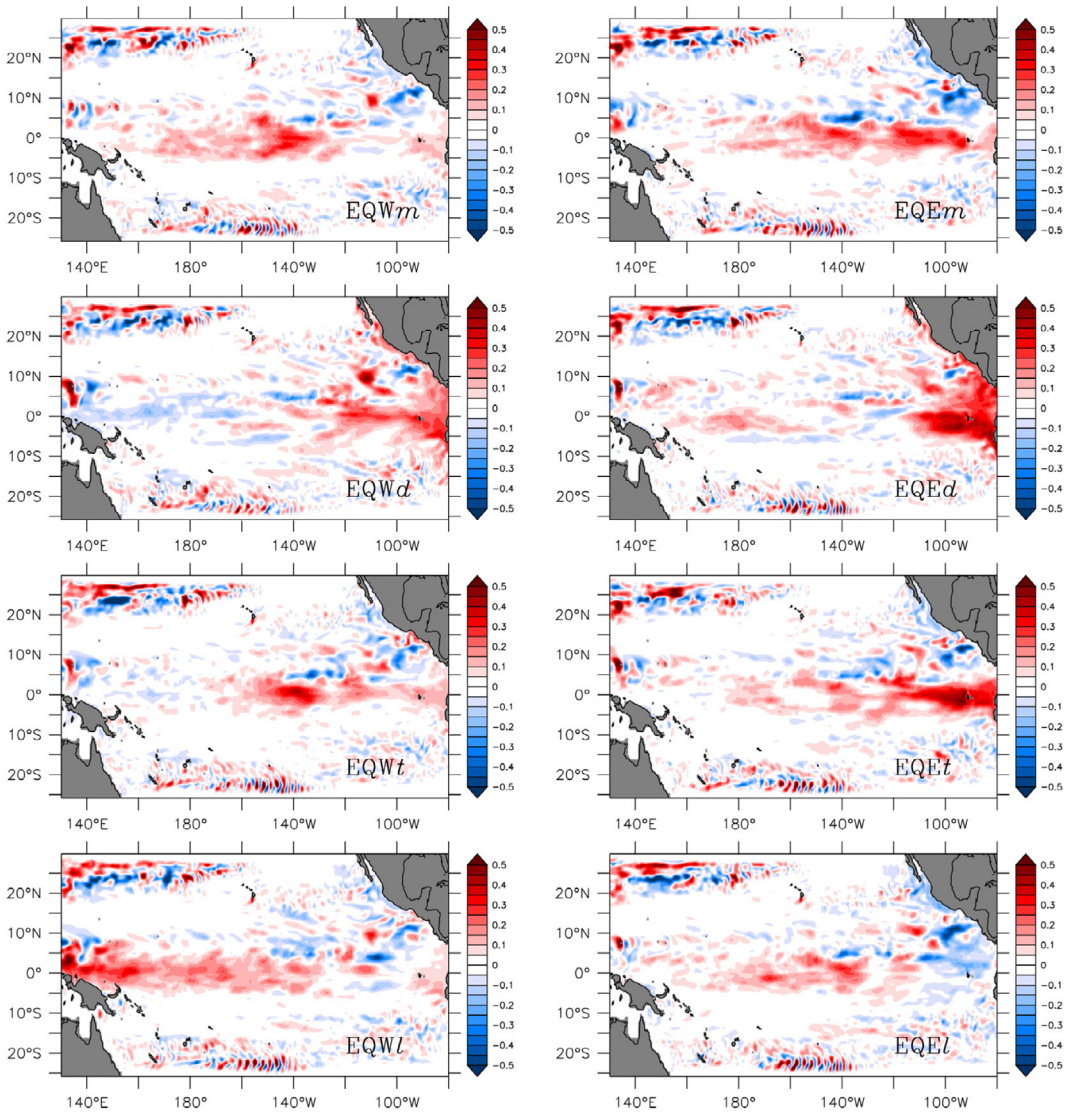


**Fig. 13.** Maps of near-surface (average in the upper 50 m) temperature anomalies (°C) during year 20 for various experiments.

they impact the location and intensity of near-surface temperatures in EEPO differently (Fig. 13). In Experiments EQW*i*, warmest anomalies occur in the central, eastern, and far-eastern ocean for Solutions EQW*m*, EQW*t*, and EQW*d*, respectively, because their warming bands occur increasingly deeper. Similarly, in Experiments EQE*i* the strongest, eastern-boundary response occurs in Solution EQE*d*, since the warming due to $\delta\kappa_z$ lies just below the surface there.

Each of the mixing profiles impacts the thermocline structure differently, with density surfaces shifted upwards (downwards) in places of cool (warm) anomalies. To illustrate the displacements, Fig. 12 plots isopycnals from the solutions (black contours) and from Experiment FB (green contours). For profiles *m* and *t*, isopycnals are lowered above the 25.0-$\sigma_\theta$ density surface and raised below it, corresponding to a sharpening of the pycnocline (Fig. 12), with the sharpening being narrower and stronger for profile *t*. For profile *d*, isopycnals shift downwards across the central portion of the thermocline, thereby deepening it. These properties are consistent with results from the 1-d model discussed in Appendix A.

A common hypothesis for the cold bias in EEPO SST in OGCM solutions is that vertical mixing is too high there, causing too much cold water to be mixed upwards to cool the surface. To test this idea, we obtained solutions with $\kappa_b$ decreased from $5 \times 10^{-5}$ cm$^2$/s to $10^{-5}$ cm$^2$/s at all depths within Regions EQW and EQE (Solutions EQW$\ell$ and EQE$\ell$, respectively; bottom panels of Figs. 12 and 13). (As might be expected, the responses in Solutions EQW$\ell$ and EQE$\ell$ are almost opposite to those of Solutions EQW and EQE; compare to Fig. 8b in Furue et al. (2015)). Although Solutions EQW$\ell$ and EQE$\ell$ also tend to sharpen the pycnocline, profiles *m* and *t* are both more effective (narrower and stronger response) in doing so (Fig. 12). In addition, significant positive anomalies in EEPO SST are present in the EQE*m*, EQE*d*, and EQE*t* solutions but not in the EQE$\ell$ solution (right panels of Fig. 13), which suggests that EEPO SST is more sensitive to vertical variations of mixing in the pycnocline than the strength of vertically uniform mixing in the region. Furthermore, EEPO SST is also highly influenced by mixing structures in the western equatorial Pacific and off-equatorial regions through wave radiation (Fig. 9 and left panels of Fig. 13). These results demonstrate that

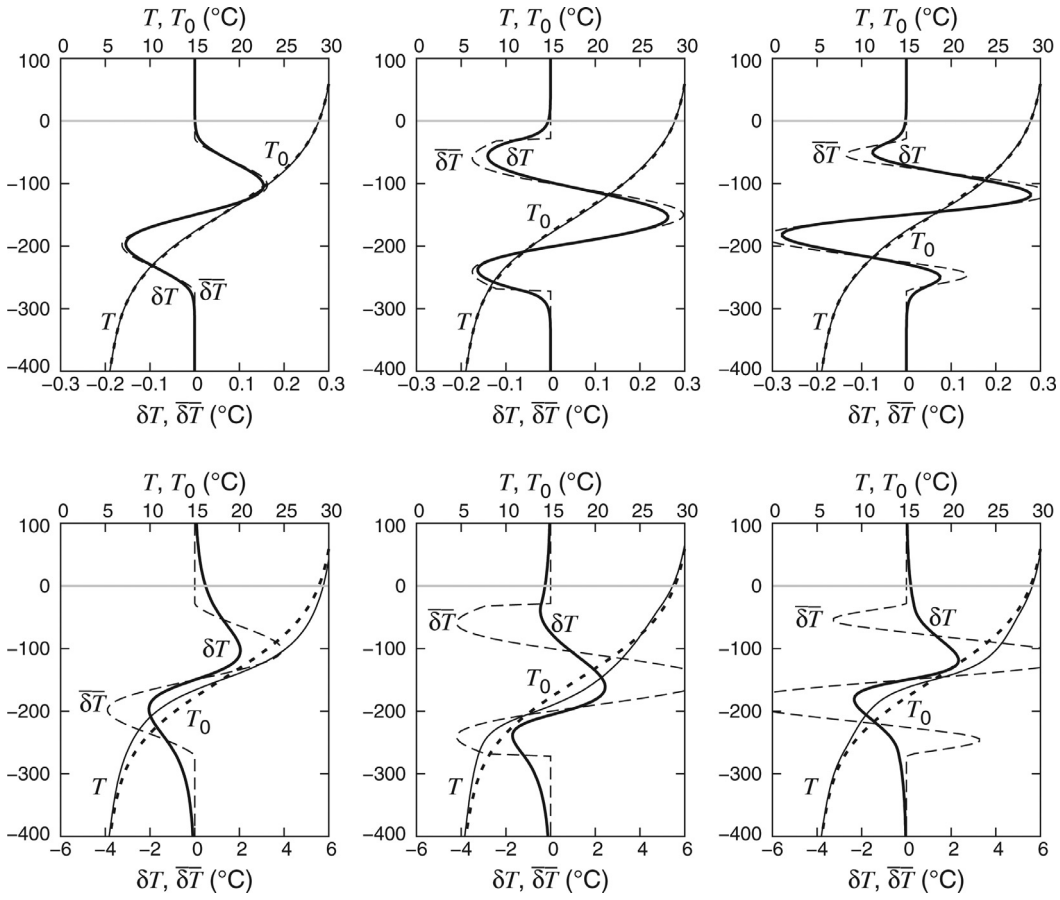


**Fig. A.1.** Temperature profiles from solutions to the steady-state version of (A.2b) when $\kappa_0 = 5 \times 10^{-5}$ m$^2$/s, $\gamma^{-1} = 30$ d (top panels) and $\gamma^{-1} = 2$ yr (bottom panels), and $\delta\kappa$ is given by profiles *m*, *d*, and *t* in Fig. 2 (left, middle, and right panels). Each panel shows: $T_0$ (thick short-dashed); steady-state responses, $T$ (thin solid) and $\delta T$ (thick solid), from the numerical solution; and $\overline{\delta T}$ (thin dashed) from solution (A.4), all with the unit °C. Top and bottom horizontal axes of each panel are scaled differently: the top axis for total temperatures, $T_0$ and $T$ (0–30 °C); and the bottom axis for temperature anomalies, $\delta T$ and $\overline{\delta T}$. Further, the bottom axes are scaled differently in the upper and lower panels (−0.3 °C to 0.3 °C and −6 °C to 6 °C, respectively). The numerical solutions are computed in a finite domain $(z_0 - h, z_0 + h)$, where $z_0 = -150$ m and $h = 400$ m, with the boundary conditions that $\delta T_z(z_0 \pm h) = 0$. The solutions are not sensitive to the locations of the artificial boundaries as long as they are sufficiently far from the region where $\delta\kappa \neq 0$.

improved specification of vertical mixing structures in the tropical and equatorial Pacific Ocean is important in reducing the cold bias of EEPO SST often seen in OGCMs.

## 5. Summary and discussion

We use an ocean model to explore how vertical diffusion influences the temperature field in the equatorial Pacific Ocean. Our approach is to change the background coefficient from a constant value $\kappa_b$ to $\kappa_b + \delta\kappa(z)$ in various subregions of the tropical Pacific, and then to determine the resulting temperature changes in the near-equilibrium response.

During the first year of adjustment, solutions develop a local temperature anomaly that results largely from the 1-d balance (1), with a similar equation for salinity. At this stage, $\delta\kappa$ generates temperature and salinity anomalies that are either associated with a density change (dynamical anomalies) or without one (spiciness anomalies); subsequently, the two anomaly types spread to remote regions by wave radiation and advection, respectively (see the schematic diagrams in Fig. 10 of Furue et al. (2015)). Eq. (1) also allows temperature anomalies to be split into those generated by $\delta\kappa_z T_z$ and $\delta\kappa T_{zz}$, the former tending to generate large anomalies because the vertical scale of $\delta\kappa$ is smaller than that of $T$.

For positive $\delta\kappa$ anomalies confined above the mid-pycnocline (profile *a* in Fig. 2), $\delta\kappa_z T_z$ in (1) tends to produce positive dynamical anomalies (bottom-right panels of Figs. 3 and 4) whereas $\delta\kappa T_{zz}$ tends to produce negative ones (middle-right panels of Figs. 3 and 4); both anomalies are still apparent in near-equilibrium solutions (Figs. 6 and 8) and spread to the equator primarily by wave radiation following the pathways as illustrated in Fig. 10 of Furue et al. (2015). The positive anomalies from all the subregions contribute to an increase of near-surface (upper 50 m) temperatures in the EEPO, owing to the surfacing of the pycnocline in that region (Fig. 9). This response differs markedly from that generated by depth-independent anomalies (Furue et al., 2015): Full-depth mixing causes EEPO warming in Solutions NW and NE, cooling in Solutions ENE, ESE, EQW, and EQE, and little change in the others (see their Fig. 9), resulting in an overall cooling of the cold-tongue in Solution FB (top-right panel of Fig. 9). We explored the impact of mixing depth, $|z_0|$, on equatorial temperatures, finding that the largest impact occurs when the density range of remote signals coincides with that of the equatorial pycnocline (Fig. 10).

For $\delta\kappa$ anomalies confined within the pycnocline (profiles *m*, *d*, and *t* in Fig. 2), the resulting temperature anomalies tend to shift the pycnocline vertically (profile *d*) or to alter its thickness (profiles *m* and *t*) (Figs. 12 and A.1). In these cases, the locally generated, equatorial temperature anomalies are dominated by the response to $\delta\kappa_z T_z$, and have both positive and negative values in depth ranges where $\delta\kappa_z \gtrless 0$ (Figs. 11 and A.1). For the chosen profiles, however, the negative anomalies do not impact near-surface

temperatures in the EEPO, because they are either too deep or too shallow (Figs. 12 and 13). Because the warming bands occur at different depths for each of the profiles, they rise to the surface at different locations, in the central, eastern, and far-eastern ocean for profiles $m$, $t$, and $d$, respectively (Figs. 12 and 13); as a result, they warm the cold tongue differently, sequentially farther to the east.

To supplement our MITgcm solutions, Appendix A reports solutions to (A.2b), which differs from (1) in that it includes terms that allow the system to adjust to a steady state. The $\gamma$ term relaxes $T$ to an externally prescribed state $T_0$, with a time scale of $\gamma^{-1}$ that varies considerably depending on the processes (wave radiation, advection, etc.) that it represents. An important result is that when the restoration by $\gamma$ is strong, the $\delta T$ profile is nearly the same as that of the forcing $(\delta\kappa T_{0z})_z$ and its equilibrium amplitude is small (see Eq. A.4); in contrast, when $\gamma$ is weak, mixing makes the profile of $\delta T$ smoother than that of the forcing and the equilibrium amplitude of $\delta T$ is large. Along the equator, where the Kelvin-wave propagation speed is large and currents are strong, $\gamma$ is large and the response remains close to $T_0$ (Fig. A.1, upper panels). In contrast, off the equator where the Rossby-wave propagation speed is slow and currents are weak, $\gamma$ is small and the equilibrium response differs from $T_0$ owing to diffusive mixing (Fig. A.1, lower panels). One implication is that the responses to $\delta\kappa$ in off-equatorial regions (Regions SW, SE, NW, and NE) tend to be larger than those in the equatorial regions (Regions EQW and EQE). These properties are mirrored in our numerical solutions.

Our results support and enhance the conclusions of the prior studies noted in Section 1. Regarding Sasaki et al. (2012), Fedorov et al. (2010), and Manucharyan et al. (2011) studies, our separation of local forcing into two parts provides a convenient way to describe the warming that occurs in their solutions, that is, it occurs almost entirely by $\delta\kappa_z T_z$. Further, we demonstrate that the remotely-generated warming signals are dynamical, and so spread to the equator via wave radiation, not by advection as suggested by Fedorov et al. (2010). Regarding the Liu et al. (2012) study, our solutions using profiles $m$, $d$, and $t$ illustrate how the depth and thickness of the equatorial thermocline, as well as near-surface temperatures in the EEPO, are sensitive to the structure of $\delta\kappa$ profiles. They therefore provide clues as to how the $\delta\kappa$ patterns that develop in their best-fit solution improve the solution. For example, their tripole pattern may be trying to sharpen the pycnocline as our profile $t$ does.

In conclusion, the solutions reported in Parts 1 and 2 of this study provide a comprehensive description of how vertical diffusion impacts the equatorial temperature structure in the upper ocean: Part 1 by Furue et al. (2015) provides a general discussion of the generation and propagation of $\delta\kappa$-induced anomalies about the ocean, and Part 2 considers upper-ocean, mixing anomalies that in prior studies have been related to specific processes. Together, they provide a useful reference, which, for example, can help in the design of improved parameterizations of $\kappa_b$ in ocean models.

## Acknowledgments

This work is supported by NASA Grant NNX10AE97G. We thank Bruce Cornuelle, Armin Köhl, Chuanyu Liu, Nidia Martínez Avellaneda, Peter Müller, Kelvin Richards, Niklas Schneider, and Detlef Stammer for fruitful discussion. Anonymous reviewers' comments helped improve the manuscript. The authors are partially supported by the Japan Agency for Marine-Earth Science and Technology (JAMSTEC), by NASA through Grant NNX07AG53G, and by NOAA through Grant NA11NMF4320128, which sponsor research at the International Pacific Research Center. The authors wish to acknowledge use of the Ferret program for analysis and graphics in this paper. Ferret is a product of NOAA's Pacific Marine Environmental Laboratory. (Information is available at http://ferret.pmel.noaa.gov/Ferret/.)

## Appendix A. Solutions to a 1-d diffusion model

As discussed in Sections 3 and 4, and in Furue et al. (2015), 1-d diffusion not only explains the initial vertical structure of $\delta T_e$ anomalies but, within their respective forcing regions, much of their equilibrium responses as well. To help interpret these responses, here we solve a 1-d diffusion equation forced by a $\delta\kappa$ change with idealized structures. (See Manucharyan et al. (2011), for a discussion of similar 1-d solutions.)

### A.1. Formulation

For simplicity, we assume that the 1-d ocean has no top or bottom, that $T$ varies linearly over the water column with the constant slope $T_z = A > 0$ except for the presence of a sharper thermocline centered on $z = z_0$, and that $\delta\kappa(z)$ variations are confined near $z = z_0$ so that $\kappa(\pm\infty) = \kappa_0$. The $T$ equation and its boundary conditions are then

$$T_t = [\kappa(z)T_z]_z - \gamma[T - T^*(z)], \quad T_z(\pm\infty) = T_z^*(\pm\infty) = A. \tag{A.1}$$

The third term in (A.1) relaxes $T$ to a background state $T^*(z)$ with a time scale $\gamma^{-1}$. Temperature $T^*(z)$ represents the state to which the ocean adjusts *without* $\kappa$, that is, it is maintained by processes (e.g., advection, wave radiation, and mixing) not included in (A.1). The specific form of $T^*(z)$ is arbitrary, provided that it satisfies the far-field condition, $T_z^*(\pm\infty) = A$, and leads to a $T_0(z)$ that is stably stratified. As discussed below, because $\gamma^{-1}$ represents effects of different processes, its magnitude varies significantly from region to region; moreover, one can expect that $\gamma$ depends on $z$, a complication that we do not consider here.

It is straightforward to solve (A.1) for $T$ for a given $T^*(z)$ profile. For our purposes, however, it is more useful to consider anomalies $\delta T$ from a "control" solution $T_0$ ($\delta T \equiv T - T_0$), where $T_0$ is the steady solution to (A.1) with $\kappa = \kappa_0$, that is,

$$\kappa_0 T_{0zz} - \gamma(T_0 - T^*) = 0, \quad T_{0z}(\pm\infty) = A. \tag{A.2a}$$

According to (A.2a), $T_0$ differs from $T^*$ in that it is the background ocean state *with* $\kappa = \kappa_0 \neq 0$. Thus, $T_0$ corresponds to Experiments CTL and FB in Sections 3 and 4, respectively. Subtracting (A.2a) from (A.1) gives

$$\delta T_t = (\delta\kappa T_{0z})_z + (\kappa\,\delta T_z)_z - \gamma\,\delta T, \quad \delta T_z(\pm\infty) = 0, \tag{A.2b}$$

where $\delta\kappa(z) \equiv \kappa(z) - \kappa_0$. Eq. (A.2b) describes the time development of $\delta T$ in response to forcing by $\delta\kappa$ of the form $(\delta\kappa T_{0z})_z$ and damping by $(\kappa\,\delta T_z)_z$ and $-\gamma\,\delta T$. Eq. (1) is (A.2b) without the smoothing and damping terms, a balance that is accurate only initially before $\delta T$ has had time to grow to an appreciable amplitude.

Solutions to (A.2b) require that $T_0$ is known. Rather than specifying $T^*$ and solving (A.2a) for $T_0$, we simply set $T_0$ to

$$T_0(z) = \Delta T\ \mathrm{erf}\left(\frac{z - z_0}{\sqrt{2}b}\right) + Az + B, \tag{A.3}$$

where $\mathrm{erf}\xi \equiv (2/\sqrt{\pi})\int_0^\xi e^{-\lambda^2}d\lambda$ is the standard error function. Solution (A.3) satisfies the required far field conditions, since the $z$-derivative of the error function is a Gaussian function, which vanishes at $z = \pm\infty$. With the parameter choices $z_0 = -150$ m, $b = 80$ m, $A = 0.01$°C/m, $B = 18$°C, and $\Delta T = 10$°C, the profile mimics the pycnocline structure in the western tropical Pacific (short-dashed curves in Fig. A.1). Although not needed, we note that (A.2a) can be easily backsolved for $T^*$.

### A.2. Solutions

It is clear in Eq. (A.2b) that $\delta T$ depends on the relative magnitudes of the damping terms. Let $b$ measure the vertical scale of the solutions; then, $\phi \equiv \kappa_0/(b^2\gamma)$ measures the relative strength of diffusive to $\gamma$ damping. With $b = 80$ m and $\kappa_0 = 5 \times 10^{-5}$ m$^2$/s (its value in Section 4), $\phi = 1$ when $\gamma^{-1} = 4$ yr. Using the method discussed at the end of this subsection, we estimate that $\gamma^{-1}$ is only about 30 days in the equatorial subregions (Regions EQE and EQW), a short time scale due to the rapid dynamical adjustment by equatorial Kelvin waves; as a result, $\phi = 0.02$ and diffusive damping is negligible. Similarly, $\gamma^{-1} = 2$ yr in the tropical regions (Regions SE, SW, NE, and NW), a much longer time owing to the slower adjustment by Rossby waves, $\phi \approx 0.5$, and the diffusive and $\gamma$ damping terms are comparable. If $\kappa_0$ is reduced to $\kappa_0 = 10^{-5}$ m$^2$/s (its value in Section 3), then values of $\phi$ are reduced by a factor of 5 and diffusive damping is weak in all our subregions. In their 1-d solutions, Manucharyan et al. (2011) used $\gamma^{-1} = 10$ yr for their tropical region.

Finding an analytic solution to (A.2b) is generally not possible, owing to $\kappa$ depending on $z$. It is possible to do so, however, when either diffusive mixing ($\phi \ll 1$) or $\gamma$ damping ($\phi \gg 1$) in negligible. When $\phi \ll 1$ and with the initial condition that $\delta T(z, 0) = 0$, the solution is

$$\delta T = \overline{\delta T}[1 - \exp(-\gamma t)], \quad \overline{\delta T} = \frac{(\delta\kappa T_{0z})_z}{\gamma}. \tag{A.4}$$

According to (A.4), at times small with respect to $\gamma^{-1}$ (A.4) reduces to $\delta T = (\delta\kappa T_{0z})_z t$, that is, the solution to (1); at large times, it adjusts to the steady-state profile, $\overline{\delta T}(z)$, which has the same vertical structure as the forcing and an amplitude proportional to $\gamma^{-1}$. For values of $\phi \lesssim 1$, we expect solutions to have a similar structure to (A.4), except somewhat smoothed by the diffusion term $(\kappa\,\delta T_z)_z$.

When $\phi \gg 1$ and $\delta T(z, 0) = 0$, the steady solution is

$$\overline{\delta T} = \int_{-\infty}^{z} \frac{\delta\kappa}{\kappa} T_{0z} dz + C, \tag{A.5}$$

where $C = -\frac{1}{2}\int_{-\infty}^{\infty}(\delta\kappa/\kappa)T_{0z}dz$. Constant $C$ is determined from the constraint that $\int_{-\infty}^{\infty}\delta T\,dz = 0$ holds for all times, which follows from a $z$-integration across the domain of the equation in (A.2b) with $\gamma = 0$, subject to the boundary conditions in (A.2b), the initial condition that $\delta T(z, 0) = 0$, and the restriction that $\delta\kappa$ is of finite extent. (It is useful to implement the constraint first in a finite domain, from $-h + z_0$ to $h + z_0$, and then to take the limit that $h \to \infty$.) Note that this choice for $C$ ensures that $\overline{\delta T}$ is antisymmetric in the far field. Since $\delta\kappa \sim \kappa$, (A.5) shows that $\overline{\delta T} \sim \Delta T_0$, a *much* larger magnitude than for (A.4), for which $\overline{\delta T} \sim \phi\Delta T_0$.

Even though (A.4) is accurate only in the equatorial subregions where $\gamma^{-1}$ is small, we also use it to estimate $\gamma$ values in off-equatorial and tropical regions. Specifically, we plot the volume average of $\delta T_e$ in a box that contains a maximum or minimum of $\delta T_e$ as a function of time, and determine $\gamma$ by best-fitting (A.4) to the time series subjectively (by eye). In practice, the method is difficult to apply because away from the equator the exponential growth of $\delta T$ is masked by mesoscale and interannual oscillations. Given this problem, the value of $\gamma^{-1} = 2$ yr noted above for tropical regions should be regarded as a rough estimate.

### A.3. Examples

Fig. A.1 plots profiles from numerical solutions to the steady-state version of (A.2b) when $\kappa_0 = 5 \times 10^{-5}$ m$^2$/s, $\gamma^{-1} = 30$ d (top panels) and 2 yr (bottom panels), and $\delta\kappa$ is given by profiles $m$, $d$, and $t$ in Fig. 2 (left, middle, and right panels). Each panel shows $T_0$, $T$, and $\delta T$ from the numerical solution, and $\overline{\delta T}$ from solutions (A.4) and (A.5). For small $\gamma^{-1}$ ($\phi = 0.02$), $\delta T$ is very similar to $\overline{\delta T}$. In contrast, for large $\gamma^{-1}$ ($\phi = 0.5$) their structures differ from $\overline{\delta T}$ owing to the stronger impact of diffusive smoothing. Note also that the amplitude of the large-$\gamma^{-1}$ solutions are much larger than their small-$\gamma^{-1}$ counterparts, roughly by the ratio of their respective $\gamma$'s.

A comparison of the $T$ and $T_0$ curves illustrates the impact of the temperature anomalies on the thermocline. In response to $\delta\kappa_m$ and $\delta\kappa_t$, $\delta T$ is higher (lower) in the upper (lower) part of the thermocline, thereby sharpening (thinning) the thermocline in $T$. The response to $\delta\kappa_t$ differs from that to $\delta\kappa_m$ in that $T$ is less affected above and below the thermocline, a consequence of the positive parts of $\delta\kappa_t$ above and below the mid-thermocline tending to cancel the anomaly generated within the thermocline. In contrast, in response to $\delta\kappa_d$, $\delta T$ is positive at the center of the thermocline with weaker negative anomalies above and below, corresponding to thermocline deepening. These properties are consistent with results from the OGCM discussed in Section 4.

Finally, it is possible to divide all the $\delta T$ curves into parts forced by $\delta\kappa T_{0zz}$ and $\delta\kappa_z T_{0z}$, that is, parts $\delta^A T$ and $\delta^B T$, respectively (not shown). Consistent with the solutions in Section 4, $|\delta^A T| \ll |\delta^B T|$, a consequence of $\delta\kappa T_{0zz}$ being weak because $\delta\kappa$ and $T_{0zz}$ do not overlap well for profiles $m$, $d$, and $t$.

## References


Bryan, F., 1987. Parameter sensitivity of primitive equation ocean general circulation models. J. Phys. Oceanogr. 17, 970–985.

Cummins, P.F., Holloway, G., Gargett, A.E., 1990. Sensitivity of the GFDL ocean general circulation model to a parameterization of vertical diffusion. J. Phys. Oceanogr. 20, 817–830.

Fedorov, A.V., Brierley, C.M., Emanuel, K., 2010. Tropical cyclones and permanent El Niño in the early Pliocene epoch. Nature 463, 1066–1071. doi:10.1038/nature08831.

Furue, R., Jia, Y., McCreary, J.P., Schneider, N., Richards, K.J., Müller, P., Cornuelle, B.D., Martínez Avellaneda, N., Stammer, D., Liu, C., Köhl, A., 2015. Impacts of regional mixing on the temperature structure in the equatorial Pacific Ocean. Part 1: Vertically uniform vertical diffusion. Ocean Modell. http://dx.doi.org/10.1016/j.ocemod.2014.10.002.

Gregg, M.C., 1976. Temperature and salinity microstructure in the Pacific equatorial undercurrent. J. Geophys. Res. 81, 1180–1196.

Gregg, M.C., Peters, H., Wesson, J.C., Oakey, N.S., Shay, T.J., 1985. Intensive measurements of turbulence and shear in the equatorial undercurrent. Nature 318, 140–144.

Jones, J.H., 1973. Vertical mixing in the equatorial undercurrent. J. Phys. Oceanogr. 3, 286–296.

Kanari, S., Kobayashi, C., Takeuchi, K., 1992. Turbulent structure in the upper layer of the western equatorial Pacific Ocean. J. Oceanogr. 48, 117–127.

Kelley, D.E., Van Scoy, K.A., 1999. A basinwide estimate of vertical mixing in the upper pycnocline: spreading of bomb tritium in the North Pacific Ocean. J. Phys. Oceanogr. 29, 1759–1771.

Köhl, A., Stammer, D., 2008. Variability of the meridional overturning in the North Atlantic from the 50-year GECCO state estimation. J. Phys. Oceanogr. 38, 1913–1930.

Köhl, A., Stammer, D., Cornuelle, B., 2007. Interannual to decadal changes in the ECCO global synthesis. J. Phys. Oceanogr. 37, 313–337.

Large, W.G., McWilliams, J., Doney, S., 1994. Oceanic vertical mixing: a review and a model with a nonlocal boundary layer parameterization. Rev. Geophys. 32, 363–403.

Large, W.G., Pond, S., 1981. Open ocean momentum flux measurements in moderate-to-strong winds. J. Phys. Oceanogr. 11, 324–336.

Large, W.G., Pond, S., 1982. Sensible and latent heat flux measurements over the ocean. J. Phys. Oceanogr. 12, 464–482 doi: 10.1175/1520-0485(1982)012⟨0464:SALHFM⟩2.0.CO;2..

Ledwell, J.R., Watson, A.J., Law, C.S., 1998. Mixing of a tracer in the pycnocline. J. Geophys. Res. 103, 21499–21529.

Liu, C., Köhl, A., Stammer, D., 2012. Adjoint-based estimation of eddy-induced tracer mixing parameters in the global ocean. J. Phys. Oceanogr. 42, 1186–1206.

Manucharyan, G.E., Brierley, C.M., Fedorov, A.V., 2011. Climate impacts of intermittent upper ocean mixing induced by tropical cyclones. J. Geophys. Res. 116, C11038. doi:10.1029/2011JC007295.

Marshall, J., Adcroft, A., Hill, C., Perelman, L., Heisey, C., 1997. A finite-volume, incompressible Navier–Stokes model for studies of the ocean on parallel computers. J. Geophys. Res. 102, 5753–5766.

Meehl, G.A., Gent, P.R., Arblaster, J.M., Otto-Bliesner, B.L., Brady, E.C., Craig, A., 2001. Factors that affect the amplitude of El Niño in global coupled climate models. Clim. Dyn. 17, 515–526.

Moum, J.N., Caldwell, D.R., Paulson, C.A., 1989. Mixing in the equatorial surface layer and thermocline. J. Geophys. Res. 94, 2005–2021.

Moum, J.N., Lien, R.-C., Perlin, A., Nash, J.D., Gregg, M.C., Wiles, P.J., 2009. Sea surface cooling at the equator by subsurface mixing in tropical instability waves. Nat. Geosci. 2, 761–765. doi:10.1038/ngeo657.

Richards, K.J., Kashino, Y., Natarov, A., Firing, E., 2012. Mixing in the western equatorial Pacific and its modulation by ENSO. Geophys. Res. Lett. 39, L02604. doi:10.1029/2011GL050439.

Richards, K.J., Xie, S.-P., Miyama, T., 2009. Vertical mixing in the ocean and its impact on the coupled ocean–atmosphere system in the eastern tropical Pacific. J. Clim. 22, 3703–3719. doi:10.1175/2009JCLI2702.1.

Sasaki, W., Richards, K.J., Luo, J.-J., 2012. Role of vertical mixing originating from small vertical scale structures above and within the equatorial thermocline in an OGCM. Ocean Modell. 57–58, 29–42.

Sasaki, W., Richards, K.J., Luo, J.-J., 2013. Impact of vertical mixing induced by small vertical scale structures above and within the equatorial thermocline on the tropical Pacific in a CGCM. Clim. Dyn. 41, 443–453.

Sriver, R.L., Goes, M., Mann, M.E., Keller, K., 2010. Climate response to tropical cyclone-induced ocean mixing in an earth system model of intermediate complexity. J. Geophys. Res. 115, C10042. doi:10.1029/2010JC006106.

Sriver, R.L., Huber, M., 2007. Observational evidence for an ocean heat pump induced by tropical cyclones. Nature 447, 577–580. doi:10.1038/nature05785.

Sriver, R.L., Huber, M., 2010. Modeled sensitivity of upper thermocline properties to tropical cyclone winds and possible feedbacks on the Hadley circulation. Geophys. Res. Lett. 37, L08704. doi:10.1029/2010GL042836.

Whalen, C.B., Talley, L.D., MacKinnon, J.A., 2012. Spatial and temporal variability of global ocean mixing inferred from Argo profiles. Geophys. Res. Lett. 39, L18612. doi:10.1029/2012GL053196.